Dynamic Control of the Shielding Effectiveness of Optically Transparent Screens

Quentin Tricas, Xavier Castel, Philippe Besnier, Claire Le Paven, Patrice Foutrel

Dynamic Control of the Shielding Effectiveness of Optically Transparent Screens

Quentin Tricas, Xavier Castel, Philippe Besnier, *Senior Member, IEEE*, Claire Le Paven, and Patrice Foutrel

***Abstract*—This article presents the design, fabrication, and characterization of an active electromagnetic shield intended to dynamically protect optical and electromagnetic sensors against high intensity radiated fields. The shield exhibits high and constant optical transparency level over the entire visible light spectrum thanks to a micrometric mesh metal thin film printed on a glass substrate. The central micrometric mesh area is separated from the peripheral ground plane of the shield by a peripheral slot. This slot is fitted out with p-i-n diodes and resistors, connecting electrically the central micrometric mesh area and the ground plane. The aim of these components is to dynamically control the shielding effectiveness of the screen, by using the conducting (ON) or blocking (OFF) states of the p-i-n diodes. Accordingly, the shielding effectiveness can be set at high level to protect the system against high intensity radiated fields, and conversely at low level to both prevent system electromagnetic self-perturbation and increase the sensitivity of the internal electromagnetic sensors. Dynamic control of the shielding effectiveness of the fabricated screen, whose optical transparency is close to 85% over the entire visible light spectrum, is fully demonstrated. A shielding effectiveness contrast ranging from 5 dB to 24 dB between the ON and OFF diode states was measured in the 2–10.5 GHz frequency range in a reverberation chamber.**

***Index Terms*—Electromagnetic shielding, high-intensity radiated fields (HIRFs), micrometric mesh metal film, optical transparency, p-i-n diode, reverberation chamber, shielding effectiveness.**

I. Introduction

HIGH-INTENSITY radiated fields (HIRFs) applied to optical and/or electromagnetic (EM) sensors can be very detrimental, creating issues such as performance and data loss, hacking, or data corruption, and even partial or total destruction of the sensors in the most extreme cases [1]–[4]. Conventional solutions to strengthen electromagnetic shielding against HIRFs imply the use of enclosures made of conductive panels, and must be adapted for the shielding screens of optical sensors. Accordingly, the shields must exhibit high optical transparency over the entire visible light spectrum to enable sensors to get optical information. Multiple technical solutions fulfilling these requirements have been published over the years [5], such as the use of ultrathin silver film [6], silver nanowires in a transparent matrix [7]–[9], conducting graphene-based hybrid films [10], indium tin oxide thin films [11], [12], or mesh metal films [13]–[15] deposited on glass, polyethylene terephthalate, or free-standing. The last solution provides high shielding effectiveness (SE) over the 2–50 GHz frequency range, coupled with high level of optical transparency (higher than 80%) over the entire visible range. It is worth noting that both performance depends on the selected mesh geometrical parameters. A previous work also demonstrated the possibility to decorrelate the SE response of the shield and its optical transparency by modifying the edge termination geometry of the mesh [13]. The measured results were in full accordance with the analytical transmission line model developed in the article. In this previous study, the SE value of the transparent shield was controlled by changing the contact impedance between the central micrometric mesh area and its peripheral radio-frequency (RF) ground. This was done by varying the number of peripheral metal ribbons that connect the two areas. Nevertheless, this shield, like all the current solutions previously described, exhibited a single SE level once produced.

Controlling the SE level according to the time fluctuations of the electromagnetic threat provides technical advantages to electronic systems. In a constraining electromagnetic environment, where HIRFs are directed toward the shield, the SE must be as high as possible, to prevent any functionality loss, or sensors and embedded electronics damage. In absence of HIRFs, the shield needs to exhibit low SE for two main reasons: 1) a metal enclosure including a screen with a high SE will have a high Q-factor. If electronics inside the enclosure radiate EM waves, a high Q-factor implies a higher risk of EM self-perturbation; 2) the transparent shield being the window through which the electromagnetic sensors collect the useful EM signals, a screen with a high SE restricts their sensitivity. In the frame of an HIRFs environment, the two previous downsides are generally neglected, as full protection against HIRFs remains the foremost priority to ensure the correct operation of the system. Without EM threat, these inconveniences must be addressed to

Manuscript received August 25, 2021; revised November 18, 2021; accepted December 28, 2021. Date of publication; date of current version. This work was supported in part by the SAFRAN Electronics and Defense under Grant 2018/1107, in part by the European Union through the European Regional Development Fund, in part by the Ministry of Higher Education and Research, in part by the Région Bretagne, and in part by the Département des Côtes d'Armor and Saint-Brieuc Armor Agglomération, through the CPER Projects 2015-2020 MATECOM and SOPHIE/STIC and Ondes. (*Corresponding author: Quentin Tricas*.)

Quentin Tricas is with the Univ Rennes, INSA Rennes, CNRS, IETR - UMR 6164, F-22000 Saint-Brieuc, France, and also with the SAFRAN Electronics and Defense, F-95610 Eragny-sur-Oise, France (e-mail: qtricas@gmail.com).

Xavier Castel, Philippe Besnier, and Claire Le Paven are with the Univ Rennes, INSA Rennes, CNRS, IETR - UMR 6164, F-35000 Rennes, France (e-mail: xavier.castel@univ-rennes1.fr; philippe.besnier@insa-rennes.fr; claire.lepaven@univ-rennes1.fr).

Patrice Foutrel is with the SAFRAN Electronics and Defense, F-95610 Eragny-sur-Oise, France (e-mail: patrice.foutrel@safrangroup.com).

Color versions of one or more figures in this article are available at https://doi.org/10.1109/TEMC.2022.3146245.

Digital Object Identifier 10.1109/TEMC.2022.3146245

further optimize the performance of such systems. A suitable solution would be an optically transparent shield whose SE can be dynamically controlled to be as high as possible in the presence of HIRFs, and as low as possible otherwise. For this specific study, a SE close to 30 dB (25 dB is tolerable) is targeted in case of interferences. Such solution would offer the optimal tradeoff between EM shielding and EM detection performance.

Surface mounted devices (SMDs) such as RF diodes [16], microelectromechanical systems (MEMS) [17], [18], nanoelectromechanical systems (NEMS) and varicaps have long been used to ensure the reconfigurability of antennas at microwaves by rerouting the RF currents and thereby adjusting their electrical lengths [19]–[21]. Furthermore, an example of active EM shield based on p-i-n diodes was presented in [22]. It was based on active frequency selective surfaces. The shield exhibited dynamic SE variation, nevertheless in narrow frequency bands and without any optical transparency property. Another concept of active EM shield based on cold plasma was described in [23]. It was a complete numerical study without any optical transparency property too. In this article, we investigate an original shielding solution based on active SMDs, which exhibits a dynamic and controlled variation of its SE on a large frequency band. This active shield presents a high optical transparency over the entire visible light spectrum, and its SE is tuned by changing the contact impedance between its central micrometric mesh area and its peripheral RF ground through switching SMDs, namely p-i-n diodes [24].

The rest of this article is organized as follows. Section II details the principle and the layout of the active shield. Fabrication process of such shield is described in Section III. Experimental results are discussed in Section V after the description of the experimental setup in Section IV. Finally, Section VI concludes this article.

II. Principle of the Active Shield

A. Design Layout

The proposed shielding screen design (see Fig. 1) is built on a 50 mm square sample of 0.7 mm-thick soda-lime glass, and is based on a metal layer separated in four main areas. First, a square micrometric mesh metal layer is located in the center of the shield. It is structured by a 10 μm-width metal strips with a 200 µm mesh pitch [see Fig. 1(a)]. Second, the central mesh is surrounded by a 0.5 mm-width metal strip. Third, a 4.8 mm-width metal strip covers the external periphery of the sample (see Fig. 1). It ensures a strong electrical contact between the sample and the Faraday cage used in the experimental part of the study (see Sections IV and V). These two metal areas are separated by a 2 mm-width slot [see Fig. 1(b)]. This slot is filled by 0.304 mm-width metal ribbons ($\times$132), 0.792 mm-spaced on the four sides of the sample. On each ribbon, a SMD resistor and a p-i-n diode will be mounted with the resistor closest to the micrometric mesh central part (see Figs. 1(b) and 2). A 1.3 mm-side metal square, electrically connected to the central micrometric mesh via a 0.709 mm-width diagonal ribbon is located in the lower left corner of the peripheral slot [see Fig. 1(c)]. This pad is used to supply direct current (dc) from an external power source to the p-i-n diodes.

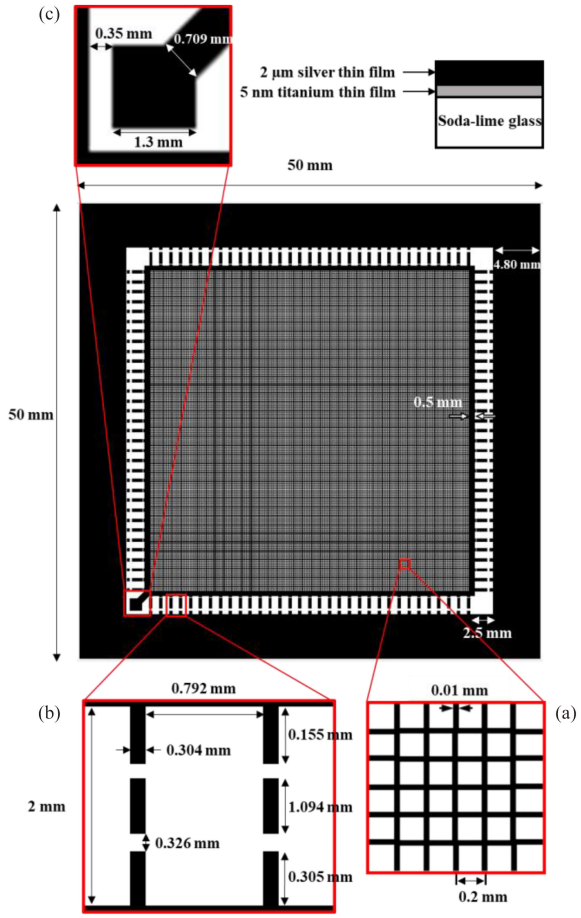

Fig. 1. (a) Schematic front and side views of the active shield, including close-ups on the mesh area, (b) the SMD embedding ribbons, and (c) the power cable connection pad.

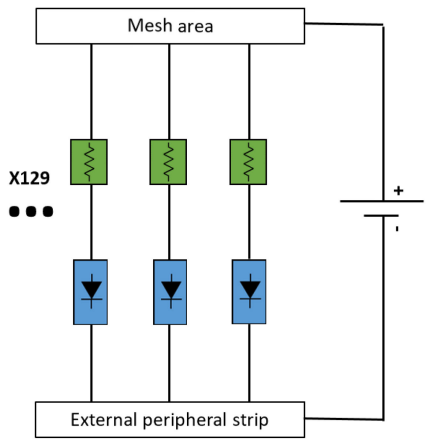

Fig. 2. Schematic drawing of the dc circuit used to supply the 132 p-i-n diodes with dc current.

B. Central Micrometric Mesh Metal Area

The complete analysis of the SE and optical transparency of the micrometric mesh metal samples designed with various geometrical parameters was extensively investigated in [25]. The SE and optical transparency of a fully micrometric mesh metal shield with identical parameters as the present one (see

Fig. 1) was measured in [13]. It displayed more than 80% of optical transparency over the entire visible light spectrum and a SE higher than 20 dB in the 2–18 GHz frequency range. These results confirmed that the selected micrometric mesh parameters will provide high optical transparency and strong shielding capabilities.

C. Peripheral Slot: Switching Diodes Effect

In a previous article [13], the SE of a micrometric mesh metal screen was statically adapted by modifying the contact impedance between the micrometric mesh and the peripheral metal strip, and thus the RF ground. On the one hand, when the number of metal ribbons connecting the central micrometric mesh area and the peripheral strip is low or null, the resulting SE is low, as the contact impedance between the mesh and the RF ground is high. On the other hand, when the density of ribbons connecting the two parts increases, the contact impedance decreases thereby improving the SE of the screen. A similar concept is investigated here, except that the physical addition or removal of metal ribbons (which implies the design and fabrication of new shields) is replaced by switching SMDs mounted on each metal ribbon, which will dynamically control the SE of the unique shielding screen.

The selected SMD needs to exhibit a low impedance in the conducting state (ON) in the 2–18 GHz frequency range and a high impedance in the blocking state (OFF) in the same frequency range. A fast switching speed is also required, as the SE of the shield needs to vary rapidly in case of HIRFs emission. Finally, a small size is also critical, as numerous SMDs have to be implemented in the peripheral slot of the shield (see Fig. 1).

A p-i-n diode (reference MA4AGFCP910 from MACOM) was selected here, as its characteristics fitted all criteria. According to the supplier technical specifications [26], its insertion loss S_{12} is equal to -34 dB in its blocking state and -0.4 dB in its conducting state at 2 GHz. Its switching speed is 2 ns, and its size is lower than 685 μm $\times$ 368 μm.

In the present shield design (see Fig. 2), when the p-i-n diodes mounted on each ribbon are not supplied with dc current (i.e., in their blocking state), the ribbons have a negligible effect on the propagation of the incident EM wave through the shield, as their impedance are extremely high. Thereby, the peripheral slot (40.40 mm $\times$ 2 mm $\times$ 4) surrounding the central mesh area is seen as almost unobstructed from the standpoint of the EM waves. Conversely, when the p-i-n diodes are supplied with dc current and switched in their conducting state, the impedance of the peripheral ribbons lowers drastically. The large peripheral slot becomes a succession of smaller ones (0.792 mm $\times$ 2 mm $\times$ 32 $\times$ 4), each spaced by a conductive ribbon providing a low impedance path for the RF current.

Peripheral slot sizes were set based on the following criteria. It is well known that an aperture of length L into an EM shield allows the transmission of an EM wave if $L \geq \frac{\lambda}{4}$, where λ is the wavelength of the EM wave [27]. Conversely, such aperture does not significantly impact the SE of the shield if $L \ll \frac{\lambda}{4}$. In the present study, the lowest wavelength value achieved by the incident EM equals 16.7 mm (at 18 GHz). In the conducting state of the p-i-n diodes, peripheral slots have a length of 2 mm (and 2.5 mm in the four corners), which is $\sim$8 times smaller than the smallest EM wavelength. Hence, the SE of the shield is expected to remain high in the 2–18 GHz frequency range. Conversely, the highest wavelength value achieved by the incident EM waves equals 150 mm (at 2 GHz). In the blocking state, the peripheral area is equivalent to four larger 40.40 mm $\times$ 2 mm slots for the EM waves. The length of the slots is thus close to a quarter of the EM wavelength value at 2 GHz. Thereby, the SE of the shield is expected to significantly decrease.

Each metal ribbon is also fitted with an 8.2 Ω SMD resistor (reference YAG6435CT-ND from Yageo). Its role is to prevent any dc current imbalance between the numerous p-i-n diodes (see Fig. 2). The resistor value was selected to be close to the series resistance of the p-i-n diodes in their conducting state (up to 6 Ω at 10 GHz [26]), but low enough to minimize the contact impedance of the ribbons when the diodes are in their conducting state.

Finally, two additional shields were also designed and fabricated for reference. The first one uses the same layout as shown in Fig. 1, without any p-i-n diode and resistor. This shield will emulate the case of ideal diodes in a perfect blocking state. The second one has 132 full metal ribbons (without any gap). This shield will emulate the case of ideal diodes in a perfect conducting state.

III. Fabrication Process

A. Metal Thin Film Deposition and Etching

A 5 nm/2 μm titanium/silver (Ti/Ag) bilayer was deposited at room temperature by the RF-magnetron sputtering technique on 50 mm $\times$ 50 mm $\times$ 0.7 mm soda-lime glass substrates with a dielectric permittivity $\varepsilon_r = 5.0$ and negligible loss at the operating frequencies. The conductive pattern (see Fig. 1) was fabricated using conventional photolithography and wet etching processes. Further details are reported elsewhere [13], [25].

B. SMD Implementation

After the thin film elaboration and engraving steps, p-i-n diodes and 8.2 Ω resistors were mounted and connected to the shield using an electrically conductive die attach adhesive. A detailed picture is presented in Fig. 3(a). A 1 mm-diameter and 10 cm-length dc power wire was connected to the pad in the corner of the shield [see Fig 1(c)]. A spot of nonconductive adhesive (see blue color in Fig. 4) was also added to prevent accidental ripping of the wire.

C. 50 Ω Transmission Line

A 50 Ω transmission line was fabricated to measure the S_{12} parameter of the p-i-n diode over the entire 2–18 GHz frequency range. It consisted of a 2.312 mm-length and 200 μm-width coplanar line with a 30 μm-width gap, made of 5 nm/2 μm Ti/Ag sputtered bilayer printed on a 0.7 mm-thick Corning 1737 glass substrate ($\varepsilon_r = 5.7$ and negligible loss at the operating frequencies). Conventional photolithography and wet etching processes were used. The p-i-n diode was connected at both

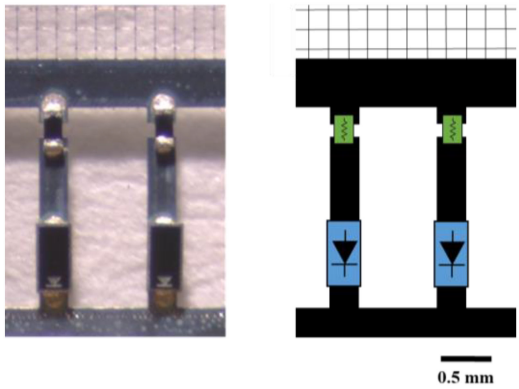

Fig. 3. (a) Detail picture of the SMDs mounted on the shield and (b) the related schematic drawing.

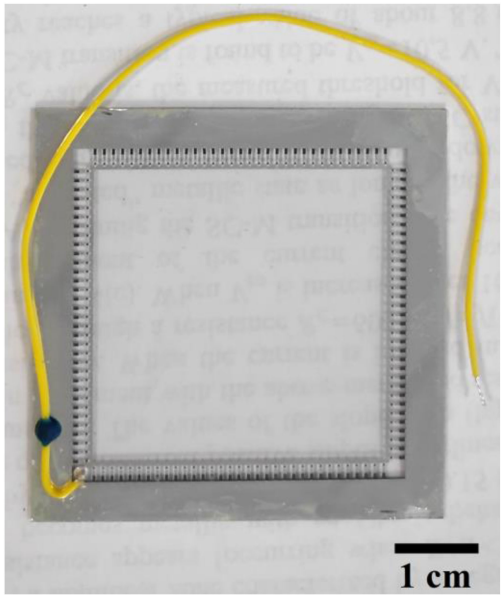

Fig. 4. Global picture of the active shield equipped with the SMDs, and the dc power wire.

ends of a 0.32 mm-width gap in the middle of the transmission line using an electrically conductive adhesive.

IV. Experimental Setup

A. Optical Transparency

Optical transparency of the central micrometric mesh area of the shield was measured in the 200–1100 nm range in normal incidence using a PerkinElmer Lambda 365 ultraviolet-visible spectrophotometer after air (blank) calibration. It is worth noting that the measured optical transparency includes the Fresnel loss of the soda-lime glass substrate (4% per side).

B. p-i-n Diode Performance

The p-i-n diode ON- and OFF-state performance was assessed in the 2–18 GHz frequency range using the 50 Ω transmission

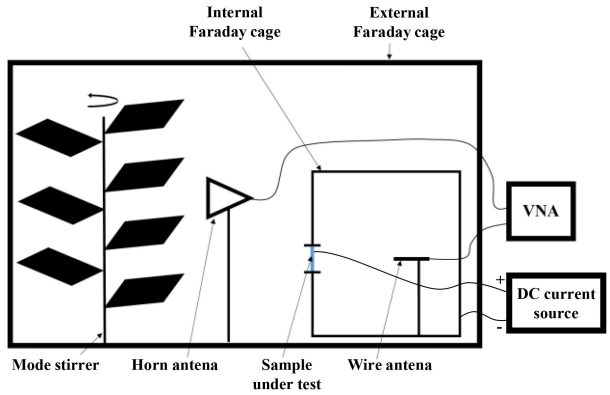

Fig. 5. Schematic view of the setup used to measure the shield SE variation versus frequency and dc current.

line previously described. The S_{12} parameter of the diode was measured with a 2 ports Vector Network Analyzer (VNA) MS4644B from Anritsu under various dc currents supplied with an external power source (Keithley 2400). The experimental setup was calibrated using the Short-Open-Load-Through method.

C. Shielding Effectiveness Measurement

SE measurements were based on the nested reverberation chamber procedure SE_3, as described in [28]. Settings used, as well as the justification of the dynamic range of the measurement setup are detailed in [25]. The procedure summarized as follows: a small Faraday cage (580 mm × 590 mm × 600 mm) with a 15 cm-length wire receiving antenna inside, was placed into a larger reverberation chamber (2.9 m × 3.7 m × 8.7 m). This large chamber also held a mode stirrer (see Fig. 5). A 3115 double-ridged transmitting horn antenna (ETS-Lindgren) was placed into the larger chamber to radiate the EM field in the 2–18 GHz frequency range. Both wire and horn antennas were connected to an external 4 ports VNA (from Rhode and Schwarz). The VNA was calibrated using a full-two-port calibration method. A square aperture was made into the Faraday cage to receive a specially designed sample-holder. Once placed, it left a 46.8-mm-side-length-square open window in the cage (see Figs. 5 and 6). The measurement process was twofold: first, the open-aperture setup (i.e., with the empty sample-holder) was assessed. Second, the shield was placed in the sample-holder, as to completely close the aperture, with the SMDs on top of the shield facing the inside of the cage. The shield was in galvanic contact with the Faraday cage through its 4.8 mm-width Ti/Ag strip. The sample-holder on its rear side was fastened with spread screws. The dc power wire of the shield was connected to a coaxial cable running from the inside of the Faraday cage [see Fig. 6(b)] to the power source located outside the large reverberation chamber. This setup was assessed under various dc currents. Comparison between the unloaded and loaded Faraday cage aperture provides the SE of the shield.

(a)

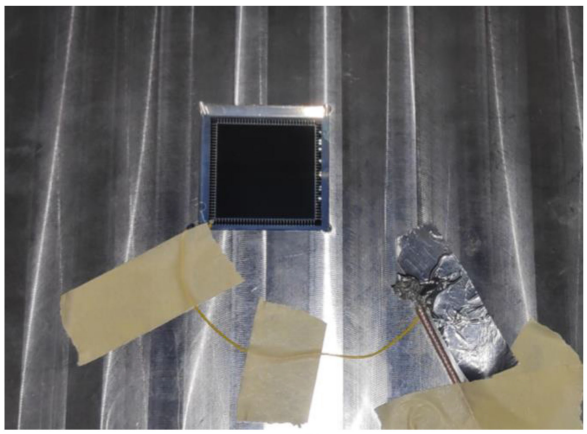

(b)

Fig. 6. (a) External picture and (b) internal picture of the Faraday cage setup used to measure the shield SE variation versus frequency and dc current.

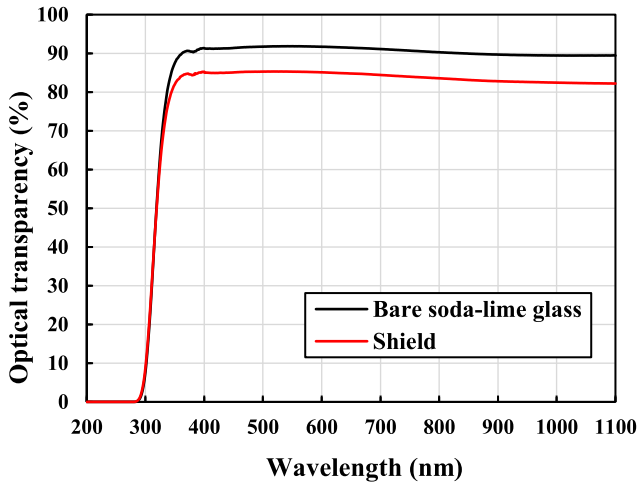

Fig. 7. Measured optical transparency versus wavelength of the central micrometric mesh Ti/Ag area of the shield. Spectrum of the bare soda-lime glass is also plotted for comparison.

V. Results and Discussion

A. Optical Transparency

The central part of the shield, namely the micrometric mesh Ti/Ag area, exhibits a measured optical transparency in the visible light spectrum equal to 84% at 400 nm, down to 83% at 800 nm whereas the bare sodo-lime glass exhibits an optical transparency of 91% and 90%, respectively (see Fig. 7). The effect of the micrometric mesh is, therefore, a reduction of 7% in transparency. It is worth noting that the bare sodo-lime glass exhibits a theoretical optical transparency equal to 92% due to the Fresnel loss. Accordingly, the theoretical optical transparency of the micrometric mesh film, computed from [13] is equal to 83.1%, in full agreement with the measured values above. Below 300 nm (ultraviolet wavelengths), the sodo-lime glass is no longer transparent explaining the curve patterns in both cases. This result demonstrates the relevance of the micrometric mesh metal layer to protect optical sensors against HIRFs without compromising on performance.

B. p-i-n Diode Performance

Measurements on the 50 Ω transmission line were carried out with three values of dc current: without power supply, under 1 mA dc current and under 10 mA dc current (see Fig. 8). The p-i-n diode exhibits a S_{12} variation of more than 14 dB at 2 GHz between its blocking state ($S_{12} = -14.5$ dB without power supply) and its conducting state ($S_{12} = -0.2$ dB under 10 mA dc current, in accordance with the supplier technical specifications), confirming thereby its switching capability. However, S_{12} variation level at higher frequency rapidly decreases (∼6 dB at 18 GHz). It is worth noting that the diode can be set in an intermediate state between its fully conducting and blocking states through its under-powering (1 mA dc current here). Accordingly, the resulting S_{12} level ranges between the abovementioned two states.

C. Shield SE Control

The SE of the shield was assessed with the p-i-n diodes in various states. First, the SE without dc current supply (i.e., p-i-n diodes in their OFF state) was measured in the 2–18 GHz frequency range. Then, the SE values were measured in the same frequency range, while dc current was supplied to the p-i-n diodes (i.e., in their ON state). A 50 mA dc current was found to be necessary and sufficient to completely switch the 132 diodes of the shield. Measurements with higher dc current values (150 mA here) showed no significant SE improvement (see Fig. 9). A large variation of SE is observed in the 2–14 GHz frequency range in between the case when no dc power supplies the p-i-n diodes (OFF state) and the case when 50 mA is provided (ON state). The SE variation between these two states reaches a maximal value of 24 dB (at 2.8 GHz) and remains significantly higher than 5 dB in the 2–10.5 GHz frequency range.

However, diodes have practically no effect on the SE variation beyond 14 GHz (SE values even being slightly worsened by the activation of the diodes). We postulate that this behavior is due to the intrinsic performance of the diodes used. Fig. 8 shows that the diode attenuates the RF signal by only 7 dB on the 50 Ω transmission line beyond 14 GHz in absence of dc current. We conclude that the selected diode is not performant enough to efficiently block RF current at high frequency, thus, why no significant SE variation is observed beyond 14 GHz.

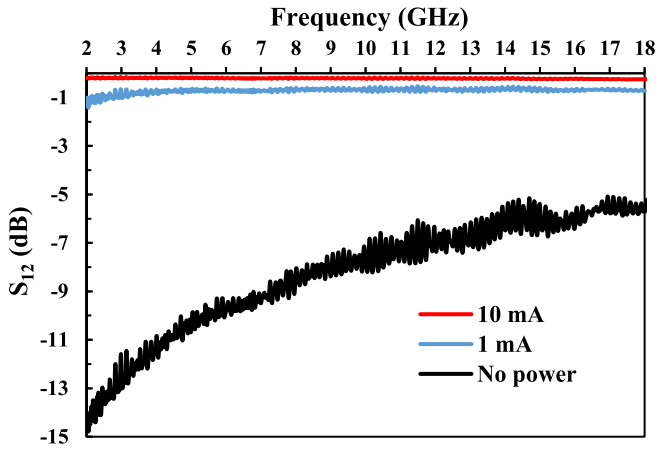

Fig. 8. S_{12} parameter variation versus frequency and dc current supply of the MA4AGFCP910 p-i-n diode implemented on a 50 Ω transmission line.

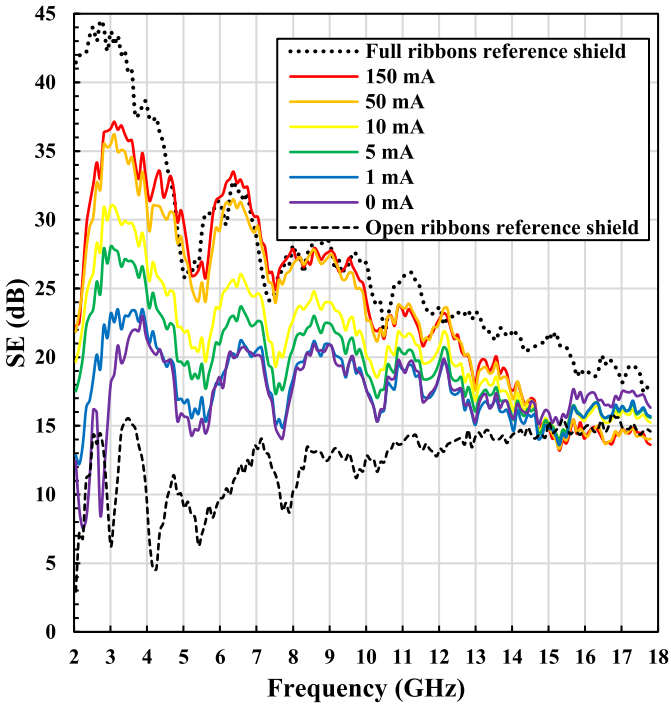

Fig. 9. Shielding effectiveness of the active shield versus frequency and dc current supply. SE of two reference shields are also plotted for comparison.

In the 2–14 GHz frequency range, we demonstrate that the shield SE is dynamically controlled. In the framework of optical/EM sensor protection, this feature can be used to increase the SE of the shield when HIRFs arise, by providing suitable dc current. In the absence of HIRFs, the SE can be lowered by not powering the p-i-n diodes. This prevents self-perturbation of the sensors by decreasing the Q-factor of their enclosure. A shield with low SE also helps to increase the sensitivity of the EM sensors.

Two reference shields (one with full Ti/Ag ribbons and the other with open Ti/Ag ribbons (without any SMD)) were also characterized at microwaves. As expected, their SE frame those of the active shield.

The SE of the reference shield with open Ti/Ag ribbons remains lower than that of the active shield without power supply. This is probably due both to a masking effect of the SMDs and the performance of the diodes in their blocking state, which present a lower impedance than the open ribbons. It is worth noting that the SE of the open ribbons reference shield is the only one that increases with frequency. This behavior is due to the capacitive coupling of the openings made into the peripheral ribbons that increases as the frequency increases. This leads to a decrease of the global contact impedance between the central micrometric mesh area and the peripheral RF metal strip, itself connected with a very low impedance to the Faraday cage. Hence, when the operating frequency increases, the SE slightly improves.

The SE of the full Ti/Ag ribbons reference shield remains higher than that of the active shield supplied with 50 mA dc current. This result stems from the low impedance of the full silver ribbons compared with that of the resistors and diodes in series. We also suspect that the dc power wire could play a role in lowering SE value at low frequency by acting as an antenna close to 2 GHz.

Finally, oscillations in SE response of the shields are observed at various frequencies, independently of the applied dc current. This phenomenon was already observed on other shield concepts measured with the same reverberation chamber [13], [25]. These oscillations are due to the aperture size (50 mm × 50 mm) in the Faraday cage. When the aperture is unloaded, its dimensions are in the same order of magnitude as the wavelength of the RF wave used to assess the SE. This makes this aperture prone to resonating, the approximation of large apertures being not applicable in the low frequency range of measurements.

D. Intermediate SE Levels Through Diodes Under-Powering

A partial switch of the p-i-n diodes from their blocking state to their conducting state can be achieved through their under-powering (see Fig. 8). Applied directly to the active shield, the under-powering of the 132 diodes (i.e., with dc current values lower than 50 mA) provides intermediate and controlled SE levels (see Fig. 9). This behavior provides a new level of freedom of the active shield with the perfect control of targeted SE values.

VI. Conclusion

The design, fabrication process, and characterization of an optically transparent EM shielding screen with tunable SE values have been investigated. The central micrometric mesh titanium/silver area of the shield exhibits an optical transparency higher than 80% over the entire visible light spectrum, while keeping a high SE. The SE variation is achieved thanks to peripheral p-i-n diodes that are controlled using dc current. Between the OFF- and ON-states of the diodes, a SE contrast of up to 24 dB is measured at 2.8 GHz and remains significantly higher than 5 dB over the 2–10.5 GHz frequency range. Furthermore, this active shield enables precise control of the SE level by adjusting the dc current supplied to the p-i-n diodes. This control process is technically simple, cost-effective, and robust. Its versatility enables its implementation in systems requiring EM shields with a dynamically controlled SE, which can be adapted to

various electromagnetic environment and specifications. Future research prospects could include the assessment of other p-i-n diode types, or SMDs. Beyond the commercial-off-the-shelf solutions, dedicated design of MEMS or NEMS could also be a research path to improve the shield SE variation amplitude, and its operating frequency band.

Acknowledgment

The authors would like to thank T. Batté from NanoRennes, Rennes, France, and J.-C. Magnard and L. Delarbre from SAFRAN Electronics and Defense, Valence, France, for the SMD implementation on the shielding screens. J. Sol from IETR at INSA Rennes, France is also warmly acknowledged for his technical support on SE measurements.

References

[1] M. G. Backstrom and K. G. Lovstrand, "Susceptibility of electronic systems to high-power microwaves: Summary of test experience," *IEEE Trans. Electromagn. Compat.*, vol. 46, no. 3, pp. 396–403, Aug. 2004, doi: 10.1109/TEMC.2004.831814.

[2] D. Nitsch, M. Camp, F. Sabath, J. L. Ter Haseborg, and H. Garbe, "Susceptibility of some electronic equipment to HPEM threats," *IEEE Trans. Electromagn. Compat.*, vol. 46, no. 3, pp. 380–389, Aug. 2004, doi: 10.1109/TEMC.2004.831842.

[3] D. F. Kune *et al.*, "Ghost talk: Mitigating EMI signal injection attacks against analog sensors," in *Proc. IEEE Symp. Secur. Privacy*, 2013, pp. 145–159, doi: 10.1109/SP.2013.20.

[4] Y. Zhang and K. Rasmussen, "Detection of electromagnetic interference attacks on sensor systems," in *Proc. IEEE Symp. Secur. Privacy*, 2020, pp. 203–216, doi: 10.1109/SP40000.2020.00001.

[5] B. Ray, S. Parmar, and S. Datar, "Flexible and transparent EMI shielding materials," in *Advanced Materials for Electromagnetic Shielding*. Hoboken, NJ, USA: Wiley, 2018, doi: 10.1002/9781119128625.ch8.

[6] H. Wang *et al.*, "Transparent ultrathin doped silver film for broadband electromagnetic interference shielding," in *Proc. IEEE MTT-S Int. Microw. Workshop Ser. Adv. Mater. Processes RF THz Appl.*, 2018, pp. 1–3, doi: 10.1109/IMWS-AMP.2018.8457129.

[7] J. Jung *et al.*, "Highly stretchable and transparent electromagnetic interference shielding film based on silver nanowire percolation network for wearable electronics applications," *ACS Appl. Mater. Interfaces*, vol. 9, no. 51, pp. 44609–44616, Dec. 2017, doi: 10.1021/acsami.7b14626.

[8] S. Lin *et al.*, "Room-temperature production of silver-nanofiber film for large-area, transparent and flexible surface electromagnetic interference shielding," *NPJ Flex. Electron.*, vol. 3, no. 1, pp. 1–8, Mar. 2019, doi: 10.1038/s41528-019-0050-8.

[9] L.-C. Jia, D.-X. Yan, X. Liu, R. Ma, H.-Y. Wu, and Z.-M. Li, "Highly efficient and reliable transparent electromagnetic interference shielding film," *ACS Appl. Mater. Interfaces*, vol. 10, no. 14, pp. 11941–11949, Apr. 2018, doi: 10.1021/acsami.8b00492.

[10] L. Ma *et al.*, "Transparent conducting graphene hybrid films to improve electromagnetic interference (EMI) shielding performance of graphene," *ACS Appl. Mater. Interfaces*, vol. 9, no. 39, pp. 34221–34229, Oct. 2017, doi: 10.1021/acsami.7b09372.

[11] J. L. Huang, B. S. Yau, C. Y. Chen, W. T. Lo, and D. F. Lii, "The electromagnetic shielding effectiveness of indium tin oxide films," *Ceram. Int.*, vol. 27, no. 3, pp. 363–365, Jan. 2001, doi: 10.1016/S0272-8842(00)00088-2.

[12] F. Colombel, X. Castel, M. Himdi, G. Legeay, S. Vigneron, and E. M. Cruz, "Ultrathin metal layer, ITO film and ITO/Cu/ITO multilayer towards transparent antenna," *IET Sci. Meas. Technol.*, vol. 3, no. 3, pp. 229–234, May 2009, doi: 10.1049/iet-smt:20080060.

[13] M. Croizer, Q. Tricas, P. Besnier, X. Castel, and P. Foutrel, "Control of shielding effectiveness of optically transparent films by modification of the edge termination geometry," *IEEE Trans. Electromagn. Compat.*, vol. 62, no. 6, pp. 2431–2440, Dec. 2020, doi: 10.1109/TEMC.2020.2982644.

[14] P. D. Tung and C. W. Jung, "High optical visibility and shielding effectiveness metal mesh film for microwave oven application," *IEEE Trans. Electromagn. Compat.*, vol. 62, no. 4, pp. 1076–1081, Aug. 2020, doi: 10.1109/TEMC.2019.2927923.

[15] Z. Jiang *et al.*, "Ultrathin, lightweight, and freestanding metallic mesh for transparent electromagnetic interference shielding," *Opt. Exp.*, vol. 27, no. 17, pp. 24194–24206, Aug. 2019, doi: 10.1364/OE.27.024194.

[16] P. Y. Qin, A. R. Weily, Y. J. Guo, T. S. Bird, and C. H. Liang, "Frequency reconfigurable quasi-Yagi folded dipole antenna," *IEEE Trans. Antennas Propag.*, vol. 58, no. 8, pp. 2742–2747, Aug. 2010, doi: 10.1109/TAP.2010.2050455.

[17] D. E. Anagnostou *et al.*, "Design, fabrication, and measurements of an RF-MEMS-based self-similar reconfigurable antenna," *IEEE Trans. Antennas Propag.*, vol. 54, no. 2, pp. 422–432, Feb. 2006, doi: 10.1109/TAP.2005.863399.

[18] A. Zohur, H. S. Mopidevi, D. Rodrigo, M. Unlu, L. Jofre, and B. Cetiner, "RF MEMS reconfigurable two-band antenna," *IEEE Antennas Wireless Propag. Lett.*, vol. 12, pp. 72–75, Jan. 2013, doi: 10.1109/LAWP.2013.2238882.

[19] R. L. Haupt and M. Lanagan, "Reconfigurable antennas," *IEEE Antennas Propag. Mag.*, vol. 55, no. 1, pp. 49–61, 2013, doi: 10.1109/MAP.2013.6474484.

[20] Y. J. Guo, P. Y. Qin, S. L. Chen, W. Lin, and R. W. Ziolkowski, "Advances in reconfigurable antenna systems facilitated by innovative technologies," *IEEE Access*, vol. 6, pp. 5780–5794, Jan. 2018, doi: 10.1109/ACCESS.2017.2789199.

[21] N. O. Parchin, H. J. Basherlou, Y. I. A. Al-Yasir, R. A. Abd-Alhameed, A. M. Abdulkhaleq, and J. M. Noras, "Recent developments of reconfigurable antennas for current and future wireless communication systems," *Electron*, vol. 8, no. 2, Feb. 2019, Art. no. 128, doi: 10.3390/electronics8020128.

[22] C. Yang, H. Li, Q. Cao, and Y. Wang, "Switchable electromagnetic shield by active frequency selective surface for LTE-2.1 GHz," *Microw. Opt. Technol. Lett.*, vol. 58, no. 3, pp. 535–540, Mar. 2016, doi: 10.1002/mop.29617.

[23] M. Liu, "Four-layer tunable wideband electromagnetic shield based on cold plasma," *IEEE Access*, vol. 8, pp. 171621–171627, Sep. 2020, doi: 10.1109/ACCESS.2020.3024550.

[24] C. Dupeyrat, P. Foutrel, P. Besnier, and X. Castel, "Optically transparent electromagnetic shield assembly," Int. Patent WO 2018/215243, Nov. 29, 2018.

[25] Y. Corredores, P. Besnier, X. Castel, J. Sol, C. Dupeyrat, and P. Foutrel, "Adjustment of shielding effectiveness, optical transmission, and sheet resistance of conducting films deposited on glass substrates," *IEEE Trans. Electromagn. Compat.*, vol. 59, no. 4, pp. 1070–1078, Aug. 2017, doi: 10.1109/TEMC.2017.2654269.

[26] "MACOM - Product Detail - MA4AGFCP910," MACOM. Accessed: Aug. 3, 2021. [Online]. Available: https://www.macom.com/products/product-detail/MA4AGFCP910

[27] C. Butler, Y. Rahmat-Samii, and R. Mittra, "Electromagnetic penetration through apertures in conducting surfaces," *IEEE Trans. Antennas Propag.*, vol. 26, no. 1, pp. 82–93, Jan. 1978, doi: 10.1109/TAP.1978.1141788.

[28] C. L. Holloway, D. A. Hill, J. Ladbury, G. Koepke, and R. Garzia, "Shielding effectiveness measurements of materials using nested reverberation chambers," *IEEE Trans. Electromagn. Compat.*, vol. 45, no. 2, pp. 350–356, May 2003, doi: 10.1109/TEMC.2003.809117.

Quentin Tricas received the diplôme d'ingénieur degree in chemistry from the European School of Chemistry, Polymers and Materials Science of Strasbourg, University of Strasbourg, Strasbourg, France in 2018 and the M.Sc. degree in functional materials and nanoscience from the University of Strasbourg, in 2018. He is currently working toward the Ph.D. degree in electronics with the Institut d´Electronique et des Technologies du numéRique (IETR, UMR-CNRS 6164) University of Rennes 1, Saint-Brieuc, France.

He was with SAFRAN Electronics and Defense in 2018. His research interests include the design, fabrication, and characterization of optically transparent electromagnetic shielding using thin film materials.

Xavier Castel received the Ph.D. degree in material science from the University of Rennes 1, Rennes, France, in 1997.

From 1999 to 2016, he was an Associate Professor with the Technological Institute of Saint-Brieuc, University of Rennes 1, Saint-Brieuc, France, and a Researcher with the Institut d'Electronique et des Technologies du numéRique (IETR, UMR-CNRS 6164), University of Rennes 1, where he was nominated as a Full Professor in 2017. He is currently the Co-Head of the Functional Materials Team with the Department of Antennas and Microwave Devices. He has authored and coauthored more than 60 international papers, more than 235 conference presentations, and holds 22 patents. His main research interests include the elaboration of advanced materials (transparent and conducting materials, superconductors, semiconductors, composite materials) for microwave applications, their physical-chemical characterizations (electrical, optical, structural, microstructural, thermal, mechanical properties, etc.) and the fabrication of the related microwave devices and antennas (by photolithographic technique, wet-etching process, lift-off process, laser micro-etching; contact molding, vacuum infusion, compression molding, and prepreg processes).

Prof. Castel is a recipient and corecipient of eight scientific awards.

Philippe Besnier (Senior Member, IEEE) received the diplôme d'ingénieur degree in electronics from école universitaire d'ingénieurs de Lillle, Lille, France, in 1990 and the Ph.D. degree in electronics from the University of Lille, Lille, France, in 1993.

Following a one-year period with ONERA, Meudon as an Assistant Scientist in the EMC division, he was with the Laboratory of Radio-Propagation and Electronics, University of Lille, as a Researcher (chargé de recherche) with the Centre National de la Recherche Scientifique (CNRS) from 1994 to 1997. From 1997 to 2002, Philippe Besnier was the Director of Centre d'Etudes et de Recherches en Protection Electromagnétique: a non-for-profit organization for research, expertise and training in EMC and related activities, based in Laval, France. He also cofounded TEKCEM in 1998, a small business company specialized in turn-key systems for EMC measurements. Back to CNRS in 2002, he has been since then with the Institut d'Electronique et des Technologies du numéRique (IETR UMR-CNRS 6164), Rennes, France. He was appointed as CNRS Senior Researcher (directeur de recherche au CNRS) in 2013. He was Co-Head of the "antennas and microwave devices" research department of the IETR between 2012 and 2016. He headed the WAVES (electromagnetic waves in complex media) team during the first semester of 2017. Since July 2017, he has been the Deputy Director with the IETR. His research interests include interference analysis on cable harnesses (including electromagnetic topology), theory and application of reverberation chambers, shielding and absorbing techniques, near-field probing, and uncertainty quantification in EMC modeling.

Claire Le Paven received the Ph.D. degree in chemistry science from the University of Rennes 1, Rennes, France, in 1994.

She completed a one-year Postdoctoral Fellowship in 1994 and 1995 with the Max Planck Institute of Stuttgart, Germany, in the H.-U. Habermeier Group. She has been an Associate Professor since 1995, first with the University of Evry Val d'Essonne, France, carrying out her research work with the Laboratory of Nanometric Multilayers directed by Pr. P. Houdy, and then from 2001, with the University of Rennes 1, France, with the Materials Department, Institut Universitaire de Technologie, Saint Brieuc. She is a Researcher with the Institut d'Electronique et des Technologies du numéRique (IETR, UMR-CNRS 6164), France. She has authored and coauthored more than 65 international papers, more than 140 conference presentations, and holds three patents. Her research interests include elaboration of innovative dielectrics and ferroelectrics materials, in ceramics and thin films forms, for telecommunication microwave applications, their physical-chemical characterizations (structural, optical, microstructural, thermal, electric, dielectric, and ferroelectric properties, etc.) and the fabrication of the related microwave devices (planar miniature and frequency agile antennas and miniature dielectric resonator antennas).

Patrice Foutrel received the Diplôme D'ingénieur degree in electronics from École Nationale Supérieure de l'Electronique et de ses Applications, Cergy, France in 1984.

He was with SAGEM, SAFRAN Group, Paris, France, in 1987. He is an Engineer with R&D with SAFRAN, Eragny, France, and an EMC Emeritus Expert with SAFRAN Group. He has been an EMC R&T Pilot since ten years. He has been involved in R&D electronics projects since 30 years.

Mr. Foutrel is an EUROCAE member WG14 and WG31